

1 **Fractional solubility of iron in mineral dust aerosols over coastal**
2 **Namibia: a link with marine biogenic emissions?**

3
4 **Karine Desboeufs¹, Paola Formenti¹, Raquel Torres-Sánchez^{2,3}, Kerstin Schepanski^{4,\$}, Jean-**
5 **Pierre Chaboureau⁵, Hendrik Andersen^{6,7}, Jan Cermak^{6,7}, Stefanie Feuerstein⁴, Benoit Laurent¹,**
6 **Danitza Klopper^{8,*}, Andreas Namwoonde⁹, Mathieu Cazaunau², Servanne Chevaillier², Anaïs**
7 **Feron^{1,%}, Cécile Mirande-Bret¹, Sylvain Triquet¹, and Stuart J. Piketh⁸**

8
9
10 ¹ Université Paris Cité and Université Paris Est Créteil, CNRS, LISA, F-75013 Paris, France

11 ² Université Paris Est Créteil and Université Paris Cité, CNRS, LISA, F-94010 Créteil, France

12 ³ CIQSO, Robert H. Grubbs Building, University of Huelva, Campus El Carmen, E21071 Huelva, Spain

13 ⁴ TROPOS, Leipzig, Germany

14 ⁵ Laboratoire d'Aérologie (LAERO), Université de Toulouse, CNRS, UT3, IRD Toulouse, France

15 ⁶ Institute of Meteorology and Climate Research, Karlsruhe Institute of Technology (KIT), Karlsruhe,
16 Germany

17 ⁷ Institute of Photogrammetry and Remote Sensing, Karlsruhe Institute of Technology (KIT), Karls-
18 ruhe, Germany

19 ⁸ North-West University, School for Geo- and Spatial Sciences, Potchefstroom, South Africa

20 ⁹ SANUMARC, University of Namibia, Henties Bay, Namibia

21
22 * Now at University of Limpopo, Department of Geography and Environmental Studies, Sovenga,
23 South Africa

24 \$ Now Institute of Meteorology, Freie Universität Berlin, Berlin, Germany

25 % Now at Université Paris-Saclay, INRAE, AgroParisTech, UMR ECOSYS, Palaiseau, France

26
27 **Corresponding author: paola.formenti@lisa.ipsl.fr**

29 **Abstract**

30 Mineral dust is the largest contributor to elemental iron in the atmosphere, and, by deposition, to the
31 oceans, where elemental iron is the main growth limiting nutrient. Southern Africa is an important
32 source at the regional scale and for the Southern Ocean, however limited knowledge is currently
33 available about the fractional solubility of iron from those sources, as well as on the atmospheric
34 processes conditioning its dissolution during deposition.

35 This paper presents the first investigation of the solubility of iron in mineral dust aerosols from 176
36 filter samples collected at the Henties Bay Aerosol Observatory (HBAO), in Namibia, from April to
37 December 2017. During the study period, 10 intense dust events occurred. Elemental iron reached
38 peak concentrations as high as $1.5 \mu\text{g m}^{-3}$, significantly higher than background levels. These events
39 are attributed to wind erosion of natural soils from the surrounding gravel plains of the Namib desert.
40 The composition of the sampled dust is found to be overall similar to that of aerosols from northern
41 Africa, but characterised by persistent and high concentrations of fluorine, which are attributed to
42 fugitive dust from mining activities and soil labouing for construction.

43 The fractional solubility of Fe (%SFe) for both the identified dust episodes and background conditions
44 ranged between 1.3 to 20 % and averaged at 7.9% ($\pm 4.1\%$) and 6.8 ($\pm 3.3\%$), respectively. Even in
45 background conditions, the iron fractional solubility was correlated to that of aluminium and silicon.
46 The solubility was lower between June and August, and increased from September onwards, during
47 the austral spring months. The relation with measured concentrations of particulate MSA (methane
48 sulfonic acid), solar irradiance and wind speed suggests a possible two-way interaction whereby ma-
49 rine biogenic emissions from the coastal Benguela upwelling to the atmosphere would increase the
50 solubility of iron-bearing dust, according to the photo-reduction processes proposed by Johansen and
51 Key (2006). The subsequent deposition of soluble iron could act to further enhance marine biogenic
52 emissions. This first investigation points to the west coast of southern Africa as a complex and dy-
53 namic environment with multiple processes and active exchanges between the atmosphere and the
54 Atlantic Ocean, requiring further research.

55

56 **Keywords:** aerosols, mineral dust, water-soluble Fe, atmospheric processing, marine biogenic emis-
57 sions

58 1. Introduction

59 Through the processes of atmospheric transport and deposition, mineral dust is known to provide
60 nutrients and metals to the terrestrial and marine ecosystems (Hooper et al., 2019; Ventura et al.,
61 2021). Amongst those, mineral dust provides iron (Jickells et al., 2005), which plays a major role for
62 the primary productivity of the nutrient-limited oceans, modulating the marine carbon cycle (Hooper
63 et al., 2019) as well as that of key continental ecosystems such as the Amazon rainforest (Reichholf,
64 1986).

65 To date, much attention has been paid to the soluble Fe in mineral dust emitted from arid and semi-
66 arid areas in the northern Hemisphere, in particular the Saharan and Chinese deserts (e.g. Baker et
67 al., 2006; Paris et al., 2010; Takahashi et al., 2011; Rodriguez et al., 2021), where emissions are the
68 most intense (Tegen and Schepanski, 2009). Nonetheless, the southern Hemisphere accounts for
69 approximately 10% of the global atmospheric dust loading (Kok et al., 2017). Large sources are found
70 in southern Africa, mostly in Namibia (Kalahari and Namib deserts, Etosha Pan, numerous ephemeral
71 riverbeds along the Namibian coastline) and Botswana (Makgadikgadi Pan) (Prospero et al., 2002;
72 Bryant et al., 2007; Mahowald et al., 2003; Ginoux et al., 2012; Vickery and Eckardt, 2013; Von Holdt
73 et al., 2017).

74 Previous research has shown that the long-range transport of dust emitted from southern African
75 sources can reach the south-eastern Atlantic and the Indian Oceans (Swap et al., 1996; Jickells et
76 al., 2005; Bhattachan et al., 2012; 2015; Ito and Kok, 2017). In particular, Gili et al. (2022) demon-
77 strated recently that mineral dust from Namibia can also be transported across the Southern Oceans
78 to eastern Antarctica. Furthermore, the research by Dansie et al. (2022) has suggested that mineral
79 dust from Namibia could dominate the atmospheric deposition to the coastal Benguela Upwelling
80 System (BUS), where biomass burning aerosols, a significant source of soluble Fe to the Southern
81 and Indian Oceans (Hamilton et al., 2021; Ito et al., 2021; Liu, et al., 2022), are limited by atmospheric
82 stratification (Formenti et al., 2019; Redemann et al., 2021). The inputs of Namibian (and Angola)
83 dust in the upwelled waters could also modulate the migration of skipjack tuna between Gulf of Guinea
84 and equatorial Atlantic, by contributing to support phytoplankton growth and hence upper trophic lev-
85 els in this area (Rodriguez et al., 2023).

86 There is, however, very little data available on the concentrations and composition of soluble Fe in
87 dust aerosols from southern Africa, both near the sources and over the oceans. Previous research in
88 Namibia focussed on soils and sediments (Dansie et al., 2017a; 2017b; Kanguuehi, 2021). The At-
89 lantic Meridional Transect (AMT) cruise programme conducted recurrent observations between Oc-
90 tober and March in the South Atlantic Ocean (Baker et al., 2013), while Heimbürger et al. (2013) and
91 Gao et al. (2013) report on sparse measurements of deposited aerosols and in rainwaters over the
92 Southern Indian Ocean.

93 Within this context, this paper investigates the fractional solubility of Fe in samples of atmospheric
94 aerosol particles smaller than 10 μm in diameter collected in 2017 at the Henties Bay Aerosols Ob-
95 servatory (HBAO; 22.09°S, 14.26°E) on the Namibian coast. In section 2 we outline the experimental
96 and analytical methodology for elemental and water-soluble analysis of ions and metals, including
97 iron. We also provide the definition of fractional solubility and method for estimating the total dust
98 mass. We introduce the supporting tools used to evaluate the source regions of the collected mineral
99 dust, their pathways during transport, and the presence of fog, a recurrent feature on coastal Namibia
100 favouring multi-phase ageing processes. Section 3 provides the results of the analysis. We present
101 the iron soluble concentrations and solubility, and explore their links to the load, emission area and
102 transport of mineral dust, as well as atmospheric processing. Section 4 discusses the observations,
103 suggesting that the fractional solubility of iron in the Namibian dust is higher when the MSA, a tracer
104 of marine biogenic emissions, is also detected in highest concentrations. This points to the photo-
105 oxidation of DMS as a process for increasing the Fe solubility, and suggests a possible positive feed-
106 back loop of the iron fertilisation by dust to the ocean. Section 5 summarizes the findings and suggests
107 directions for future research.

108

109 **2. Methodology**

110 **2.1. Study area**

111 The Henties Bay Aerosol Observatory (HBAO, 22.09°S, 14.26°E; <http://www.hbao.cnrs.fr/>, last ac-
112 cess: 10 October 2022) is located at the Sam Nujoma Marine and Coastal Resources Research Cen-
113 tre (SANUMARC) of the University of Namibia in Henties Bay, Namibia (**Fig 1**).



114

115 **Fig 1.** Location of Henties Bay Aerosol Observatory (HBAO, red star) and main dust source regions (©
 116 Google Maps). The position of Walvis Bay (blue dot), the major harbour in the area, and the Wlotzkabaken
 117 meteorological station (blue star) are also indicated.

118

119 Three kilometers to the south of the University campus hosting HBAO is the small town of Henties
 120 Bay, with no industrial activity and very little traffic, and approximately 170 km north from Walvis Bay,
 121 the major harbour in Namibia. Directly east of HBAO are the Namibian gravel plains, which are one
 122 of the dominant features of the Namib desert together with the sand dunes. Approximately 100 m to
 123 the north is the Omaruru riverbed, one of the coastal sources of mineral dust identified by Vickery and
 124 Eckardt (2013).

125 Our previous results show that, at the surface level, the atmosphere at HBAO is a receptor of different
 126 air masses dominated by marine aerosols, but also the seasonal occurrence of light-absorbing aerosols
 127 from biomass burning or pollution in northern wind regimes, and mineral dust detected episodically
 128 from various wind directions (Formenti et al., 2018; Klopper et al., 2020, hereafter KL20).

129 **2.2. Sample collection and analysis**

130 Aerosol particles smaller than 10 μm in aerodynamic diameter (PM_{10}) were collected by an automated
 131 sampler (model Partisol Plus 2025i, Thermo Fisher Scientific, Waltham, MA USA) on 47 mm What-
 132 man Nuclepore polycarbonate filters (1- μm pore size). The air was drawn through a certified sampling
 133 inlet (Rupprecht and Patashnick, Albany, New York, USA) located at approximately 30 m above
 134 ground and operated at a flow rate of 1 $\text{m}^3 \text{h}^{-1}$. Samples were collected for 9 hours during the daytime
 135 (from 9:00 to 18:00 UTC time) and night-time (21:00 to 06:00 UTC time) for 12 non-consecutive weeks

136 from April to December 2017 (7-14 April, 26 April-3 May, 19-26 May, 07-14 July, 2-9 August, 15-22
137 August, 18-25 September, 02-09 October, 31 October-7 November, 13-20 November, 28 November-
138 04 December, 12-19 December). In total, 176 samples (+ 13 blanks, one per week of sampling) were
139 collected.

140 The elemental analysis of 24 elements from Na to Pb and including some major tracers of mineral
141 dust (Fe, Al and Si) was performed at the LISA laboratory by Wavelength-dispersive X-ray fluores-
142 cence (WD-XRF) using a PW-2404 spectrometer (Panalytical, Almelo, Netherlands), as detailed by
143 KL20. The total mass concentration per element x will be referred to as TX.

144 The measured elemental concentrations are used to calculate the estimated dust mass (*EDM*) ac-
145 cording to Lide (1992) as

$$146 \quad EDM = 1.12 \times \{1.658 \times [\text{nss-Mg}] + 1.889 \times [\text{Al}] + 2.139 \times [\text{Si}] + 1.399 \times [\text{nss-Ca}] + 1.668 \times [\text{Ti}] + 1.582 \\ 147 \quad \quad \quad \times [\text{Mn}] + (0.5 \times 1.286 + 0.5 \times 1.429 + 0.47 \times 1.204) \times [\text{Fe}]\} \quad (1)$$

148

149 where, as explained by KL20, nss-Mg and nss-Ca represent the non-sea salt fractions of Mg and Ca,
150 respectively.

151 The analysis of the water-soluble fraction was also performed at LISA. Individual filters were placed
152 in 20 mL of ultrapure water (MilliQ® 18.2 MΩ.cm) for 30 minutes. The solution was filtered (Nuclepore
153 polycarbonate filters with 0.2µm pore size) then divided into two sub-samples. One half was analysed
154 by Ion Chromatography (IC) using a Metrohm IC 850 device equipped with a column MetrosepA supp
155 7 (250/4.0 mm) for anions and with a Metrosep C4 (250/4.0 mm) for cations. The IC analysis provided
156 the concentrations of the following water-soluble ions: F⁻, Cl⁻, NO₃⁻, SO₄²⁻, formate, acetate, oxalate,
157 MSA⁻ (methanesulfonic acid), Na⁺, NH₄⁺, K⁺, Ca²⁺ and Mg²⁺. A calibration with certified standard multi-
158 ions solutions of concentrations ranging from 5 to 5000 ppb was performed and the uncertainty of the
159 analysis was estimated to be 5% (KL20).

160 The second half of the solution was acidified to 1% with ultrapure nitric acid (HNO₃) and analysed by
161 Inductively Coupled Plasma-Atomic Emission Spectroscopy (ICP-AES) using a Spectro ARCOS
162 Ametek® ICP-AES and by High-resolution Inductively Coupled Plasma-Mass Spectrometry (HR-ICP-
163 MS) using a Neptune Plus™ instrument by Thermo Scientific™. The calibration curve was performed
164 using standard multi-element solutions ranging from 2 to 1000 ppb for ICP-AES and 1 to 1000 ppt for
165 HR-ICP-MS (Desboeufs et al., 2022). These analyses provided the dissolved mass concentrations
166 (DX) of 25 water-soluble metals and metalloids, including Fe, Al, and Si. All sample concentrations
167 were corrected using the filter blanks for each sampling period.

168 Based on those analyses, the fractional solubility (%SX) representing the percentage solubility value
169 was calculated as

170

171

$$\%SX = 100 \times DX/TX \quad (2)$$

172

173 with DX and TX, the dissolved and total elemental concentration respectively.

174 Here, a leaching protocol using ultrapure water (UPW) was used to simulate wet deposition of parti-
175 cles, since the wet deposition dominates the total iron supply in the Southern Atlantic Ocean (Chance
176 et al., 2015). Moreover, the UPW leach enables the chemical reaction between iron with organic or
177 inorganic ligands, naturally dissolved from the particulate aerosols into rain droplets. However, it is
178 known that the extraction protocol modulates dissolution process and hence the values of iron frac-
179 tional solubility, in particular the estimates using UPW are higher in comparison to these one using
180 seawater, but lower than the acidic, buffered or reduction agent leach (Perron et al., 2020).

181 **2.3. Ancillary data**

182 Maps of the emission fluxes of mineral dust were calculated using the dust emission model described
183 by Feuerstein and Schepanski (2019), driven with hourly 10m wind fields at a $0.1^\circ \times 0.1^\circ$ grid from
184 the European Centre for Medium-range Weather Forecasts (ECMWF). The dust emission parame-
185 terisation follows Marticorena and Bergametti (1995). Additional information on the soil type was taken
186 from the ISRC soil data set (FAO/IIASA/ISRIC/ISSCAS/JRC, 2012) and information on the aerody-
187 namic roughness length was obtained from POLDER/ADEOS surface products following the works
188 of Marticorena et al. (2004) and Laurent et al. (2005). The MODIS monthly vegetation product
189 (MYD13A3 v6) was used to describe the vegetation cover, while the vegetation type was defined
190 using the BIOME4 database (Kaplan et al., 2003). We additionally differentiated between different
191 dust source types (alluvial fines, dunes and sand sheets) which allowed us to reflect the source di-
192 versity over Namibia and thus the spatial diversity in the soil's susceptibility to wind erosion. This layer
193 was compiled following Feuerstein and Schepanski (2019) using MODIS surface reflectance
194 (MOD09A1 v6). A MODIS retrieved map on surface water cover was used to eliminate flooded areas
195 as active dust sources.

196 Back-trajectories of the air masses during the dust event were calculated from Meso-NH model (ver-
197 sion 5.3). The model set-up is similar to the one used for the AErosols, RadiatiOn and CLOuds in
198 southern Africa (AEROCLO-sA) field campaign (Formenti et al. 2019) and related case studies (Fla-
199 mant et al. 2022; Chaboureau et al. 2022). In short, the model was run on a 5 km grid covering the
200 southern tip of Africa and 67 stretched levels spaced by 60 m close to the surface and 600 m at high
201 altitude. Meso-NH was run for 24 h for each dust event using initial and boundary conditions provided
202 by the ECMWF operational analysis. Emission, transport and deposition of dust is described by the
203 scheme of Grini et al. (2006). Back trajectories were computed online using three passive tracers

204 initialized with the 3D-field of their initial conditions. Further details on the dust prognostic scheme,
205 the backward trajectories and the physical parameterizations are given in Chaboureau et al. (2022).

206 The presence of fog and low clouds (FLC) along the Namibian coastline during dust events was an-
207 alysed using an existing satellite-based fog and low-cloud data set (Andersen et al., 2019). The FLC
208 detection algorithm used to create this data set was developed and validated specifically for this re-
209 gion. The algorithm is based on infrared observations from the Spinning Enhanced Visible and Infra-
210 red Imager (SEVIRI) aboard the geostationary Meteosat Second Generation (MSG) satellites, making
211 use of both spectral and textural information. The FLC product is available at the native spatial and
212 temporal resolutions of the SEVIRI sensor (3 km nadir, every 15 minutes), as described in Andersen
213 and Cermak (2018). The FLC product does not specifically distinguish between fog and low clouds
214 but captures the coastal boundary-layer cloud regime typical for the region and at HBAO that could
215 interact with mineral dust. It has been shown to be consistent with synoptic-scale atmospheric dy-
216 namics (Andersen et al. 2020). The FLC data are used to calculate maps of average fog and low
217 cloud coverage for the time periods of all dust events given in Table 1.

218 Observations of the local meteorology, including measurements of air temperature, relative humidity
219 and fog, at the nearby Wlotzkasbaken meteorological station (22.31°S, 14.45°E, 73 m asl, see **Fig.**
220 **1**) part of the Southern African Science Service Centre for Climate Change and Adaptive Land Man-
221 agement (SASSCAL) ObservationNet (<https://www.sasscal.org/>; last accessed 14/04/2023), are
222 used.

223

224 **3. Results**

225 **3.1. Description of the dust episodes**

226 The dataset discussed in this paper is based on 176 aerosol samples collected at HBAO, 42 of which
227 were associated with 10 dust episodes. As detailed by KL20, events of mineral dust were identified
228 as peaks in the time series of the mass concentrations of Al and non-sea-salt Ca²⁺ (nss-Ca²⁺). The
229 dust episodes investigated in this study are a subset of those presented by KL20, we therefore use
230 their naming convention to facilitate the connections between the two papers (**Table 1**). In the follow-
231 ing, we refer to samples collected during the dust episodes as “dust”. Samples collected outside the
232 dust events will be indicated as “background”.

233

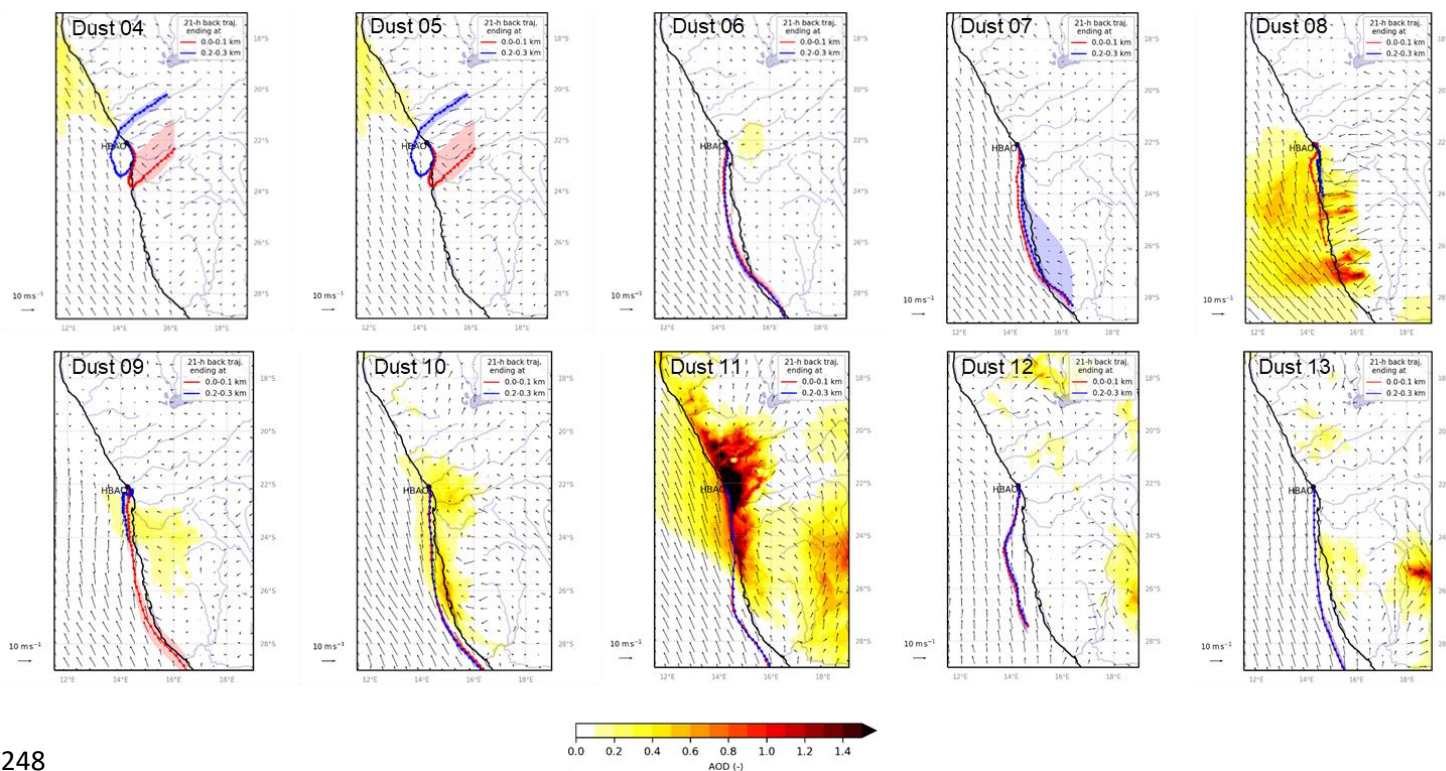
234 **Table 1.** *Dates of dust events identified at HBAO from May to December 2017, following KL20. The number of*
235 *samples collected during each episode is indicated in the column called “N”. The average air temperature,*
236 *relative humidity, wind speed and direction recorded at the nearby meteorological station in Wlotzkasbaken are*
237 *reported. The maxima wind speed and corresponding direction are indicated in brackets in the corresponding*
238 *columns. The average EDM is reported with in brackets the maximum of EDM during the event.*

Episode identifier	Start and end date (UTC)	N	Air temperature (°C)	RH (%)	Wind speed	Wind direction (degN)	EDM
--------------------	--------------------------	---	----------------------	--------	------------	-----------------------	-----

					(m s ⁻¹)		(μg m ⁻³)
Dust 04	19/05 09h – 20/05 18h	3	17.7	73.7	2.7 (6.2)	186 (185)	13 (14)
Dust 05	24/05 21h – 26/05 09h	3	18.1	63.3	2.3 (6.3)	183 (188)	21 (42)
Dust 06	11/07 09h – 13/07 09h	4	13.2	82.9	1.2 (5.4)	235 (193)	27 (45)
Dust 07	04/08 21h – 06/08 09h	4	12.5	87.0	1.2 (5.4)	233 (201)	10 (16)
Dust 08	17/08 21h – 19/08 09 h	4	11.9	80.6	1.3 (4.6)	324(129)	18 (21)
Dust 09	23/09 21h – 24/09 18h	2	15.6	84.3	3.1 (6.2)	309 (330)	11 (17)
Dust 10	05/10 21h – 08/10 09h	8	14.0	74.6	2.1 (5.9)	249 (228)	14 (23)
Dust 11	15/11 09h – 18/11 09h	6	16.7	66.1	3.2 (11.7)	231 (232)	31 (56)
Dust 12	30/11 09h – 01/12 18h	3	16.7	78.1	1.9 (5.7)	244 (195)	2 (3)
Dust 13	15/12 09h – 19/12 09h	7	16.9	76.9	2.9 (6.5)	252 (238)	10 (19)

239

240 The dust episodes were long-lasting (generally a few days). The dynamic of the emissive areas, air
241 mass transport and fog coverage during the episodes (**Fig. 2 and S1**) is driven by the synoptic circu-
242 lation, which, in southern Africa, is primarily affected by the high-pressure belt under the descending
243 limb of the Hadley cell (Tyson and Preston-Whyte, 2014). The maps of dust emission fluxes and the
244 air mass back-trajectories reflect this seasonality. During the first part of the year (episodes Dust 04
245 to 05), dust emissions originated from the gravel plains and the Etosha pan north of HBAO. During
246 this time of the year the transport to HBAO below 300 m asl was north- to south-easterly originating
247 inland from the coast.



248

249 **Fig 2.** Maps of dust optical depth (shading) and 10-m wind (vector) overlaid by pathway of 21-hour air mass
250 back trajectories ending in the first 100 m (red line) and between 200 and 300 m (blue line) above HBAO for
251 dust episodes, as calculated by the Meso-NH model (version 5.3). Dots are plotted every hour and shadings
252 around these lines are the interquartile ranges for latitudes.

253

254 From July onwards, the active source areas were identified in the southern gravel plains, Namib sand
255 dunes and Kalahari Desert (this former only for Dust 11 to 13). Air mass transport was southerly and
256 travelled over the sea and along the coastline. It is worth noticing that all the air masses experienced
257 maritime air during their last hours of transport, including the episodes Dust 04 and 05 associated
258 with berg wind conditions, due to the coastal low that develops to the west of HBAO.

259 The formation of fog events at Henties Bay is also highly seasonal. The frequency of occurrence of
260 fog events is highest during austral winter at the coast, whereas lifted stratus clouds dominate during
261 austral summer, when overall FLC occurrence peaks. The occurrence of fog over Namibia correspond
262 to the advection of low-level clouds which is modulated both by local meteorology along the coastline
263 of Namibia (trade winds) and synoptic-scale radiative processes (Spirig et al., 2019; Andersen et al.,
264 2019; 2020). Henceforth, as shown in Fig. S1, the presence of fog and low clouds correlates with
265 wind directions and aerosol source regions. Overall, three episodes (Dust 04, Dust 05 and Dust 11 in
266 April, May and November, respectively) occurred in fog-free or low-fog conditions. The remaining
267 episodes were characterised by extensive fog and low cloud coverage throughout the study area. The
268 meteorological observations at the nearby Wlotzkasbaken station (**Fig. S2**) confirm these findings,
269 and show in particular that the relative humidity always exceeded 60 %, and 80 % when fog or low
270 clouds were present (Table 1). As a consequence, the aerosol can be considered deliquescent even
271 in the fog-free conditions. The seasonality is also observed in the average downwelling solar irradi-
272 ance, with the lowest values during July and September, associated with austral winter. Finally, it is
273 interesting to note that the fog-free conditions, associated with the predominance of continental air
274 masses, corresponded to the highest estimated dust mass (EDM), possibly because of the reduced
275 wet removal during transport and the increase of emission fluxes with the decrease of soil moisture
276 (Kok et al., 2014), but possibly also because of the high wind speed prevailing during these conditions,
277 which in principle, enhances both dust emissions and transport (Table 1).

278 **3.2. Iron solubility**

279 The total and dissolved concentrations, and fractional solubility of Fe, Al and Si, during the dust epi-
280 sodes are reported in **Table 2**, where they are compared to background conditions. For iron, the
281 average values over the entire sampling period are also shown.

282 **Table 2.** Average and standard deviations of water-soluble (DX), total elemental (TX) mass concentrations and
283 fractional solubility (%SX) for Fe, Al and Si at HBAO measured for the total period and during the dust and
284 background events from April to December 2017. Concentrations values are expressed in ng m^{-3} , while frac-
285 tional solubility is expressed in percent. The numbers of considered samples is presented between the paren-
286 theses.

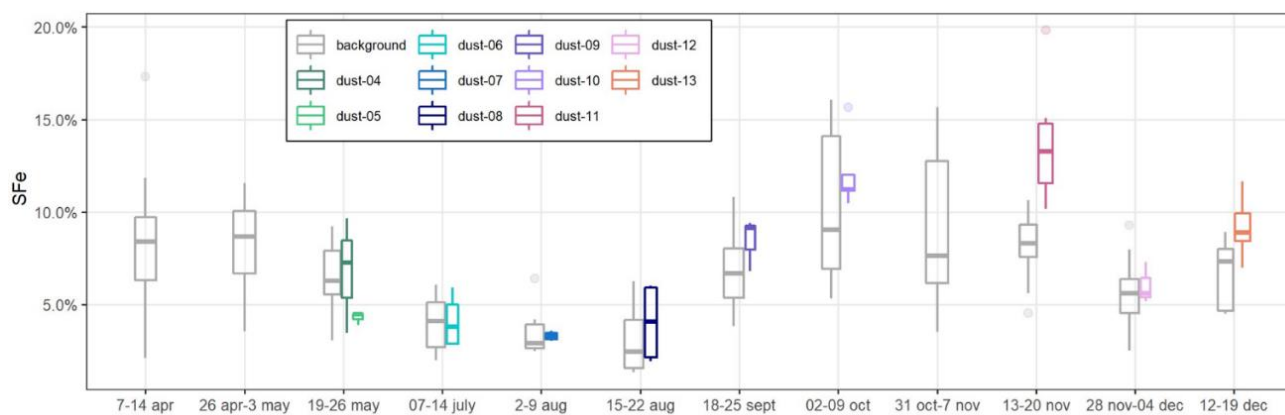
	Fe			Al		Si	
	All period	Dust	Background	Dust	Background	Dust	Background
DX	28 ± 51 (N=175)	80 ± 84 (N=42)	11 ± 10 (N=131)	322 ± 296 (N=42)	56 ± 46 (N=131)	529 ± 616 (N=42)	78 ± 83 (N=124)
TX	364 ± 482 (N=176)	955 ± 633 (N=42)	177 ± 155 (N=133)	1204 ± 870 (N=42)	284 ± 222 (N=94)	4158 ± 3037 (N=42)	776 ± 674 (N=133)
%SX	7.1 ± 3.6 (N=175)	7.9 ± 4.1 (N=42)	6.8 ± 3.3 (N=130)	27 ± 10 (N=42)	26 ± 11 (N=90)	12 ± 7 (N=42)	11 ± 8 (N=116)

287

288 The total Fe concentrations varied significantly from one episode to the other, and so did EDM, which
289 was larger than 10 $\mu\text{g m}^{-3}$ for all of them (except Dust 12) and as high as 56 $\mu\text{g m}^{-3}$ during Dust 11
290 event (Table 1). By contrast, the total Fe-to-EDM ratio was virtually constant, with an average of 5.8
291 % (± 0.6 %) for the dust events and 5.6 % ($\pm 1.1\%$) for the entire dataset. These values are quite
292 superior to usual Fe content recommended in upper continental crust models (3.5% for Taylor and
293 McLennan or 5.04 \pm 0.53 % Rudnick and gao, 2004) and estimated in Saharan dust (4.45% for
294 Guieu et al., 2002; 4.3 to 6.1% for Lafon et al., 2006 or 4.5% for Formenti et al., 2008). Keeping in
295 mind that Fe abundance is estimated, this suggests that the Namibian aerosol dust could be enriched
296 in iron in comparison to upper crust and dust provided by Saharan sources.

297 The total dissolved concentrations of Fe during the sampling period ranged from 1.5 to 427 ng m^{-3} ,
298 with a median and average of 10.5 and 28 ng m^{-3} . During the dust episodes, the average mass con-
299 centration of dissolved Fe was 80 \pm 84 ng m^{-3} , almost an order of magnitude higher than for back-
300 ground conditions (11 \pm 10 ng m^{-3}). The dissolved concentrations in dust periods are higher than
301 those observed in the South Atlantic Ocean for air masses associated with transport from continental
302 southern Africa (Baker et al., 2013; Chance et al., 2015; Baker and Jickells, 2017), which are of the
303 order as those observed at HBAO for background periods. The calculated fractional solubility of Fe
304 ranged from 1.3 to 19.8 %, with a median and average of 6.7 and 7.1 %. The average %SFe during
305 dust events (7.9 \pm 4.1%) was higher, but quite similar than in background conditions (6.8 \pm 3.3%). It
306 is interesting to note that Dust 11 event, the most intense recorded event, presents the highest %SFe
307 (between 10.2 and 19.8 % with an average at 13.8 %). Apart from this event, the average fractional
308 solubility seems to be independent of the EDM. Excluding this event, the average solubility of Fe for
309 dust event (6.9 % \pm 3.3 %) is equivalent to the one for background samples. The uniformity of iron
310 solubility values between background and dust periods contrasted with the observations made in
311 regions where the dust influence is sporadic and the origin of Fe is associated to various sources (e.g.
312 Shelley et al., 2018). That is consistent with a main dust source of iron in our samples, as indicated
313 in KL20. For both conditions, the observed range of variability is high and consistent with previous
314 observations over the Southern Atlantic Ocean (2.4-20 %, Baker et al., 2013; 1.3-22 %, Chance et
315 al., 2015), and the Southern Indian Ocean (0.76-27 %, Gao et al., 2013), using acetate buffer leach

316 at pH 4.7 (0.4 μ m) which can extract 1.4 times more Fe than UPW protocol (Perron et al., 2020).
 317 Moreover, the measured iron fractional solubility is significantly higher than obtained from dissolution
 318 experiments, with an identical protocol, of mineral dust aerosol samples collected on filters after la-
 319 boratory generation from the soils collected in Namibian sources (< 1%; Formenti et al., in preparation,
 320 2024).

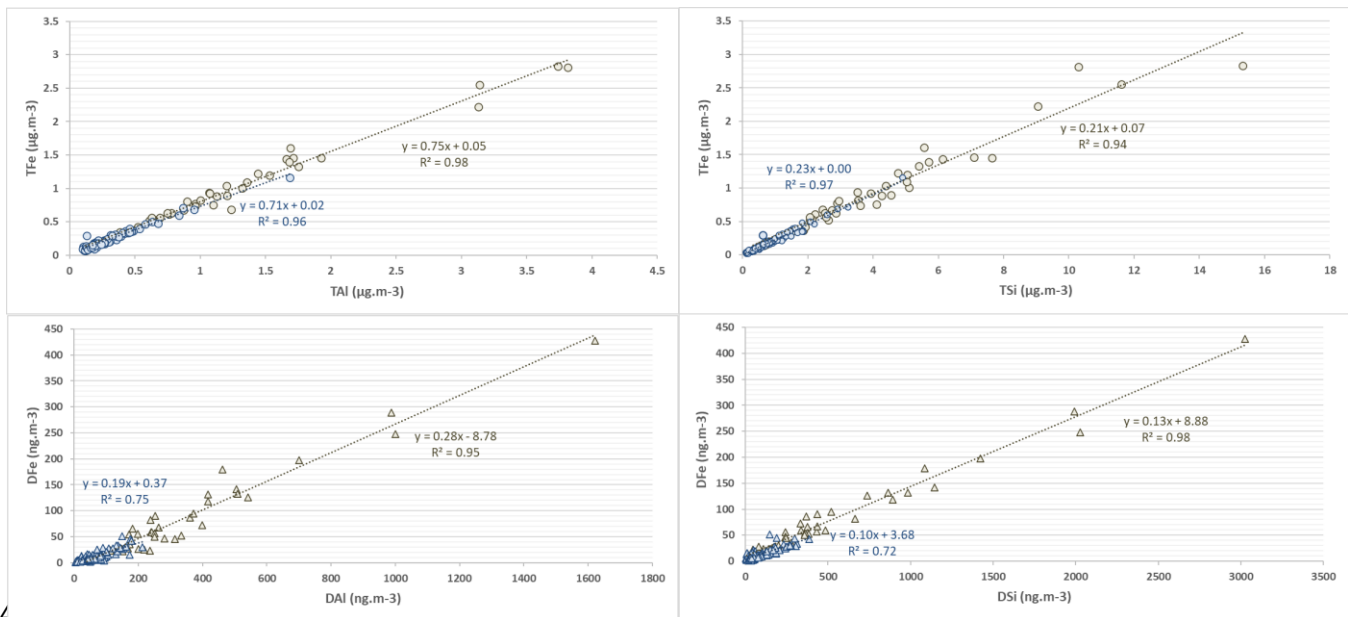


321

322 **Fig.3:** Temporal variability of %SFe average for dust and background samples during the different periods of
 323 sampling. In the box plots, the box indicates the interquartile range, i.e. the 25th and the 75th percentile, and
 324 the line within the box marks the median. The whiskers indicate the quartiles ± 1.5 times the interquartile range.
 325 Points above and below the whiskers indicate outliers outside the 10th and 90th percentile.

326

327 The temporal variability of %SFe is presented in **Fig. 3**, where dust and background episodes are
 328 shown separately. The temporal variability is similar during dust and background conditions. The
 329 highest %SFe occurred during austral spring (October-November), and in particular during episode
 330 Dust 11 from 13 to 20 November 2017, when the average %SFe reached 13.8 %. The %SFe was
 331 quite similar along the year between dust and background, except between 13-20 November where
 332 the iron solubilities during Dust 11 event was very superior to the one of background samples, and to
 333 a lesser extent, in September (Dust 09) and December (Dust 13).



334

335

336 **Fig. 4.** Scatterplot of TFe with respect to TAl and TSi (top panels) and DFe with respect to DAl and DSi (bot-
 337 tom panels) for dust (sand dots and triangles) and background events (blue dots and triangles). The Pearson
 338 coefficient are shown for both.

339

340 **Fig. 4** represents the correlations of Fe with Al and Si, both for the total and the dissolved concentra-
 341 tions. For both dust and background samples, the total Fe concentration is linearly correlated with
 342 total Al ($R^2=0.98$ and 0.96 , slope= 0.75 and 0.71 , for dust and background conditions respectively)
 343 and total Si ($R^2=0.94$ and 0.97 , slope= 0.21 and 0.23 , respectively). The slopes are consistent with
 344 typical Fe/Al and Fe/Si ratios found in desert dust from northern Africa (Formenti et al., 2011; Shelley
 345 et al., 2014), confirming the main crustal origin of Fe during all the sampling periods. Likewise, the
 346 concentrations of dissolved iron (DFe) show a strong linear correlation with both DAl and DSi, for both
 347 for dust and background events ($R^2=0.96$ and 0.75 with respect to DAl and $R^2=0.98$ and 0.73 with
 348 respect to DSi). The slopes for Al and Si are also comparable (0.19 and 0.28 for DAl and 0.10 and
 349 0.13 for DSi, respectively in dust and in background events). A very strong linear correlation was also
 350 observed between DFe and DTi ($R^2=0.96$ and 0.84 ; not shown), another unique marker of mineral
 351 dust. Significant correlations of soluble concentrations for several elements associated with mineral
 352 dust (Fe, Al, Si, Ti) have been previously obtained in remote aerosols over ocean area (Baker et al.,
 353 2016). Additionally, DFe during dust events correlate very closely with F^- ($R^2=0.94$, not shown), which
 354 has been indicated by KL20 as being emitted in the atmosphere by the wind erosion as well as the
 355 labouing of the Namibia soil, rich in fluoride mineral deposits.

356 4. Discussion

357 Several studies have showed that variations in aerosol Fe solubility could result from the source/com-
 358 position of the aerosols. As a matter of fact, the Fe solubility has been linked to the iron mineralogy

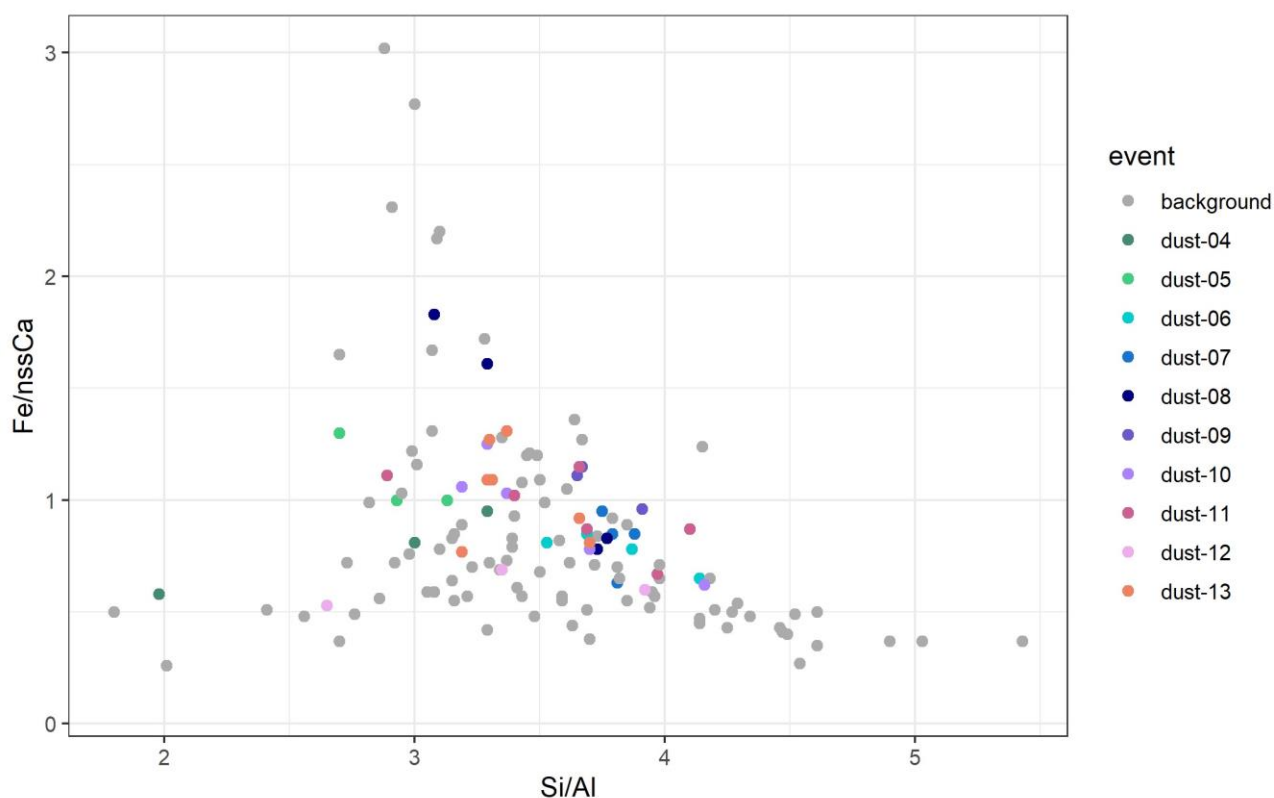
359 (Journet et al., 2008) and has been shown being lower for African crustal sources than in continen-
360 tal/anthropogenic sources (Desboeufs et al., 2005; Sholkovitz et al., 2009; Shelley et al., 2018). The
361 iron fractional solubility in mineral dust is also affected by source mixing (Paris et al., 2010; Desboeufs
362 et al., 2005), by (photo)chemical processing with acids or organic ligands during atmospheric
363 transport (Paris et al., 2011, Paris et Desboeufs, 2013; Wozniak et al., 2013; Swan and Ivey, 2021)
364 and by the increase of surface area to volume ratio due to size changes during transport (Baker &
365 Jickells, 2006; Marcotte et al., 2020).

366 In the following sections, we discuss these possible factors to explain the seasonality and the ex-
367 tended range of variability of the fraction Fe solubility in HBAO samples. The possible increase of
368 surface area to volume ratio during transport (Baker and Jickells, 2006; Marcotte et al., 2020) will not
369 be discussed because of lack of appropriate observations of the size distribution. Because of the
370 similar transport time suggested by back trajectories (Fig.2), it is likely that particle size distribution
371 would be similar from one event to the other.

372 **4.1. Influence of dust composition**

373 Close to dust source, iron solubility could be mainly conditioned by the mineralogical composition of
374 dust (Journet et al., 2008, Formenti et al., 2014). Considering that soluble Fe-bearing aerosols were
375 issued from mineral dust for all the samples, the seasonality of dust emission sources (see 3.1) could
376 be a factor explaining the seasonality of %SFe (and other elements associated to mineral dust). **Fig.**
377 **5** shows the scatter plot of the elemental mass ratio of Fe/nss-Ca²⁺ and Si/Al, previously used for
378 northern Africa dust to distinguish aerosol dust from source areas enriched in clays or iron oxides to
379 soils rich in quartz or carbonates (Formenti et al., 2014). Specific to Namibia, because of the strong
380 link between nss-Ca²⁺ and fluorine, the Fe/nss-Ca²⁺ ratio may also to distinguish dust influenced by
381 fluorspar mining.

382



383

384 **Fig 5.** Scatterplot of $Fe/nss-Ca^{2+}$ and Si/Al mass ratios for the samples collected at HBAO in period May-
 385 December 2017. Values obtained for samples collected during the dust events are represented as colored dots.
 386 Values for samples collected outside those events (background) are represented as grey dots.

387

388 Figure 5 indicates that the range of variability of both $Fe/nss-Ca^{2+}$ and Si/Al ratios is small when con-
 389 sidering dust events only. The elemental ratios of samples collected during the background periods
 390 are rather similar to dust events during a same sampling period, except for Si/Al for the period be-
 391 tween 19-26 May and for $Fe/nss-Ca^{2+}$ for the samples of 18-25 September, when significant differ-
 392 ences, not really explicable and not inducing a significant difference in the %SFe values are observed
 393 (**Fig. S3**).

394 The values for ambient dust measured at HBAO are consistent with those of the previous field obser-
 395 vations in Namibia (Annegarn et al., 1983; Eltayeb et al., 1993), but also with values reported by
 396 Caponi et al. (2017) for laboratory-aerosolised dust from two soils collected on the Namibian gravel
 397 plains. This is in agreement of the indications of the emission maps (**Fig. 2**), showing significant emis-
 398 sions in the gravel plains. The absence of seasonal cycle in the elemental composition illustrated in
 399 **Fig. S3** suggests that the seasonal change from northern to southern sources does not induce a
 400 change in the composition of the aerosol dust sampled at HBAO, which is consistent with the fact that
 401 the northern and the southern gravel plains of Namibia have similar mineralogy (Heine and Vökel,
 402 2010). This suggests that the mineralogical composition of mineral dust should not be a discriminating
 403 factor explaining the seasonality of the iron solubility observed at HBAO.

404 4.2. Evidence of processing by marine biogenic emissions

405 The atmospheric (in-cloud) processing associated with secondary aerosol production may increase
406 the fractional solubility of Fe during transport (Takahashi et al., 2011; Rodríguez et al., 2021). This
407 has also been shown for Al and Ti (Baker et al., 2020). The chemical processing could include both
408 acidic and ligand-promoted dissolution (Desboeufs et al., 2001, Longo et al., 2016, Tao et al., 2019).
409 Oxalic acid has previously been used as a proxy for organic ligand-mediated iron dissolution pro-
410 cesses because it is the most abundant species in the atmosphere and is the most effective ligand in
411 promoting iron dissolution (Baker et al., 2020; Hamilton et al., 2021). However, several secondary
412 compounds, such as carboxylate ligands and marine secondary products derived from dimethyl sul-
413 fide (DMS) oxidation, have been identified as playing a role in increasing the soluble fraction of iron
414 from mineral aerosols (Johansen and Key, 2006; Paris et al., 2011; Paris and Desboeufs, 2013; Woz-
415 niak et al., 2013 and 2015). The increase of ligands-promoted dissolution is attributed to photochem-
416 ical reduction of Fe(III) in Fe (II) (Siefert et al., 1994; Johansen and Key, 2006).

417 To investigate these aspects, the mass concentrations of the ionic compounds (oxalate, formate,
418 MSA, NO_3^- , NH_4^+ and nss-SO_4^{2-}) implied in the secondary aerosol production, measured at HBAO
419 during dust and background periods are reported in **Table 3**.

420

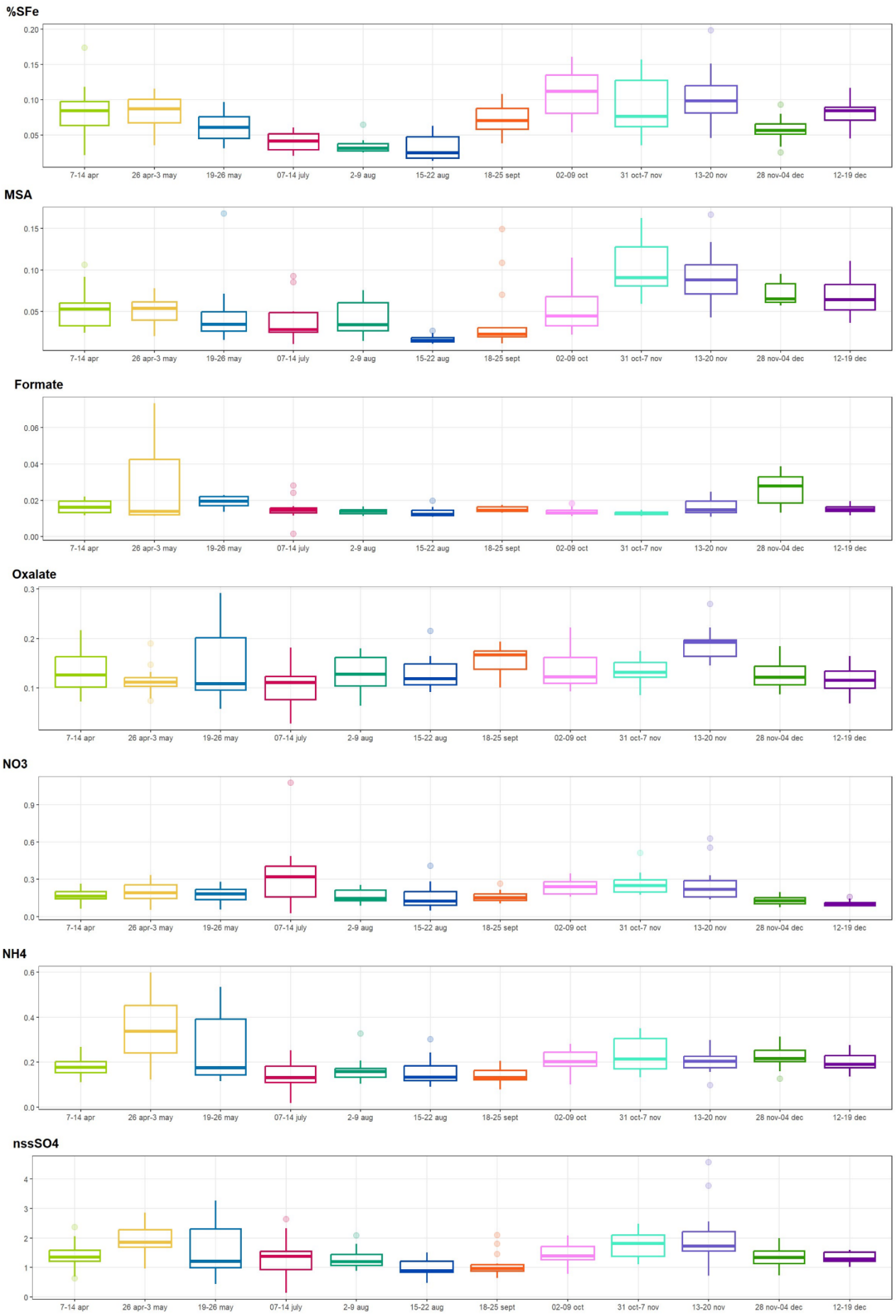
421 **Table 3.** Average and standard deviations of mass concentrations of water-soluble ions measured at HBAO during dust and
422 background events from May to December 2017. Concentrations are expressed in ng m^{-3} . The number of samples pertaining
423 to each occurrence is indicated in brackets.

	Dust	Background
nss-SO_4^{2-}	1795 ± 762 (N = 42)	1366 ± 505 (N=132)
Oxalate	155 ± 53 (N = 42)	127 ± 35 (N = 132)
Formate	18 ± 6 (N = 40)	16 ± 9 (N = 105)
MSA	64 ± 37 (N=36)	56 ± 36 (N=114)
NO_3^-	205 ± 79 (N=42)	200 ± 138 (N=132)
NH_4^+	192 ± 71 (N=42)	207 ± 98 (N=132)

424

425 Oxalate was the most abundant organic compound, followed by MSA, a secondary product of DMS
426 oxidation and a unique particulate tracer of the primary marine biogenic activity (Andreae et al., 1995).
427 On average, organic compounds were equally concentrated in dust and background events. Amongst
428 inorganic species, nss-SO_4^{2-} was the most concentrated compound, with higher values during the
429 dust events than during the background period.

430

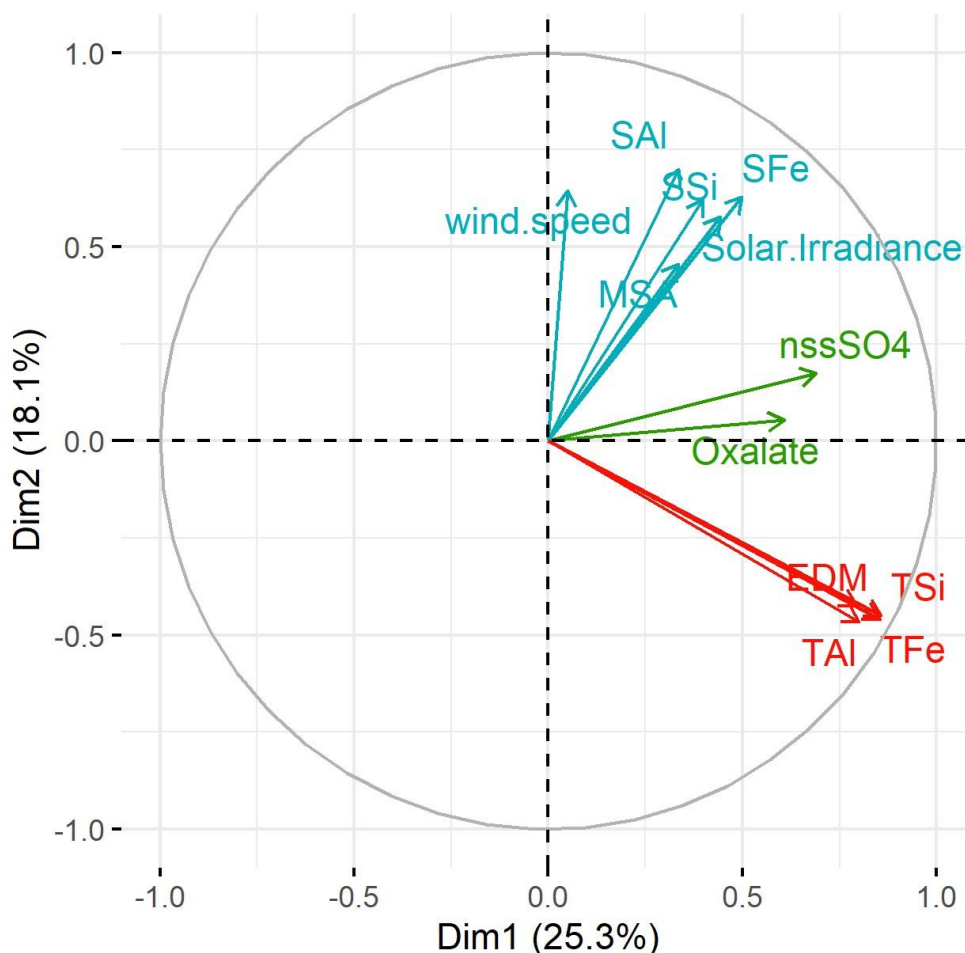


432 **Fig. 6.** Box-plots of the averages of %SFe and secondary organic and inorganic compounds mass concentrations ($\mu\text{g m}^{-3}$)
433 for the sampling periods including all the samples (dust + background). Boxes and whiskers as in Fig. 2.

434

435 Their detailed time series are shown in **Fig 6**, where it is compared to that of the iron fractional solu-
436 bility. There is no clear seasonal cycle for any of the ionic compounds, with the exception of MSA,
437 which shows a similar time variability than %SFe. MSA concentrations were lowest between May and
438 August (average $38.0 \pm 28.0 \text{ ng m}^{-3}$), while higher concentrations were measured from September to
439 December ($72.7 \pm 38.1 \text{ ng m}^{-3}$). These differences are also observed for the dust cases only. The
440 average MSA concentration was $40.6 \pm 23.4 \text{ ng m}^{-3}$ for Dust 04 to Dust 08 episodes. It increased to
441 $77.7 \pm 35.3 \text{ ng m}^{-3}$, almost a factor of 2 between episodes Dust 09 and Dust 13. The mass concen-
442 trations and the seasonal cycle of MSA are related with the proximity of the strong coastal upwelling
443 by the Benguela current (Formenti et al., 2019; KL20). The maximum concentration of MSA (106.2
444 ng m^{-3}) was measured during episode Dust 11, which is also the time of the highest SFe% observa-
445 tion. This episode was also characterised by the highest oxalate, nss- SO_4^{2-} and NO_3^- concentrations.
446 However, no clear correlation between the %SFe and the secondary compounds concentrations can
447 be found in our data (**Fig. S4**). In order to statistically explore the potential links between %SFe and
448 various these concentrations, **Fig. 7** shows the correspondence plot between total Fe, Al and Si, and
449 their respective fractional solubility, the measured secondary compounds and the meteorological con-
450 ditions during sampling obtained from Principal Component Analysis (PCA) for all the samples. The
451 variables correlated in time are grouped together (the closer they are in the circle, the stronger the
452 correlation) whereas the variables which are anti-correlated are situated on the opposite side of the
453 plot origin.

454



455 **Fig 7.** PCA analysis performed from the database including %SX, TX, EDM, secondary ions concentrations and meteorological parameters. The colour of variables by groups is defined by a clustering algorithm, tending to find clusters of comparable spatial extent. Each colour corresponds to a cluster of parameters which evolve in the same way. Formate, nitrate, ammonium, acetate, humidity, and wind speed are not visible in the plot showing that they are not significantly correlated with the other parameters (i.e. their squared cosine < 0.4).

460

461 The PCA plot (Fig.7) emphasizes 3 groups of dependent parameters: 1. a high correlation between
 462 total Fe, Al and Si concentrations and dust loading (EDM), as previously identified in Table 1 and
 463 Fig.3, 2. a relation between oxalate and nss-SO₄²⁻ concentrations, suggesting a common chemical
 464 process of formation, and 3.the dependence between %SFe (%SAI and %SSi), the MSA concentra-
 465 tions, the solar irradiance and to a lesser extent with the wind speed. While it is expected that the
 466 emission of mineral dust occurs when the wind speed is high, the correlation of %SFe with wind speed
 467 is rather surprising since the %SFe is independent of the dust load (Fig. 2 and 7). **Fig. S4** in the
 468 supplementary material present the plots between %SFe, MSA concentrations, solar irradiance and
 469 wind speed for background and dust events. The correlation between the wind speed and the MSA
 470 concentrations (Fig. S4) is consistent with Andreae et al. (1995), who demonstrated how, in this area
 471 due to persistent phytoplankton bloom, the atmospheric concentrations of dimethylsulphide (DMS),

472 the gaseous precursors of MSA, depend on the sea-to-air flux, in turn is determined by the concen-
473 trations in the ocean water and the surface wind speed..

474 As previously mentioned, Johansen and Key (2006) showed an increase of dissolution of ferrihydrite,
475 a proxy of iron(oxy)hydroxide found in desert mineral dust, by photolysis of the Fe(III)-MSIA (methane
476 sulfinic acid) complex, producing MSA and soluble Fe. Zhuang et al. (1992) proposed an increase of
477 iron dissolution by the acidification of aerosol particles associated with dimethylsulphide (DMS) oxi-
478 dation. Here, the link between the Fe fractional solubility, solar irradiance and MSA is in agreement
479 with the photo-reduction dissolution of Fe by MSA condensation on Fe-bearing dust. Thus, we attrib-
480 ute the iron fractional solubility seasonality observed at HBAO both to solar irradiance and MSA tem-
481 poral evolution via this process. It is interesting to note that due to the high correlation between %SFe
482 and %SAI and %SSi, the photochemical processes could also impact the solubility of all element-
483 bearing dust.

484 **4.3. Link to other sources of iron and oxalate**

485 Formenti et al. (2018) have shown that in the Austral winter, when the synoptic circulation is domi-
486 nantly anti-cyclonic, air masses laden with light-absorbing aerosols either from ship pollution or bio-
487 mass burning can be transported to HBAO (Formenti et al., 2018). However, the lowest Fe solubility
488 (< 5%) was measured in July and August 2017, and no correlation between the %SFe and the percent
489 mass fraction of iron from sources other than dust can be found in our data (not shown).

490 The mass apportionment of iron reported by KL20 indicates that, during the dust events and the
491 background periods, respectively, 7% and 29% of the mass of total elemental Fe was not associated
492 to mineral dust, but rather to a factor indicated as “ammonium-neutralised component”, mostly char-
493 acterised by secondary species, and non-sea-salt potassium (nss-K⁺). The PMF analysis indicated
494 that the “ammonium-neutralised component” was associated to photo-oxidation of marine biogenic
495 emission but also episodically to biomass burning. This component includes oxalate, the most con-
496 centrated organic species at HBAO, and the strongest of the organic ligands promoting the photo-
497 reduction of iron in mineral dust, henceforth the increase of its fractional solubility (Paris and
498 Desboeufs, 2013). Surprisingly, excepted individual cases (Dust 13), our analysis does not show this
499 strong link (Fig. 7), and indeed, contrary to the SFe%, the oxalate concentrations measured at HBAO
500 was practically constant with time (in average 0.14±/− 0.04 μg.m^{−3}). The possible pathways of oxalate
501 formation in this complex atmosphere are numerous through the year, from natural and anthropogenic
502 sources (marine, heavy-oil combustion, biomass burning) and in-cloud and photo-oxidative processes
503 (Baboukas et al., 2000; Myriokefalitakis et al., 2011).

504 **5. Concluding remarks**

505 For the first time, the fractional solubility of Fe in airborne atmospheric aerosols smaller than 10 μm
506 in diameter is investigated along the west coast of Namibia, in southern Africa, a critical region for the
507 global climate.

508 Ten intense episodes of transport of mineral dust from aeolian erosion were identified from the anal-
509 ysis of aerosol samples collected between May and December 2017 at the Henties Bay Aerosol Ob-
510 servatory (HBAO). Based on modelling and measurements, source regions were identified both in the
511 northern and southern gravel plains. Our data do not provide any evidence of the possible contribution
512 of dust from coastal riverbeds, which are considered to be frequent sources of atmospheric dust and
513 soluble iron in the region (Vickery et al., 2013; Von Holdt et al., 2017; Dansie et al., 2017a; 2017b).
514 The total iron represents, on average, 5.8 % (± 0.6 %) of the total dust mass, and that the average
515 water-soluble Fe fractional solubility is 6.9 % (± 3.3 %). These values should be useful to atmospheric
516 models estimating the dust-borne input of soluble Fe from the gravel plains in Namibia to the sur-
517 rounding oceans.

518 The seasonal increase of the iron fractional solubility is associated to that of the concentrations of
519 MSA and correlated to meteorological parameters such as the wind speed and the surface solar
520 irradiance. Our observations support the role of photo-chemical processes in the dissolution of Fe in
521 our samples, and suggest that the oxidation of the marine biogenic emissions from the northern Ben-
522 guela upwelling, favoured under high wind speed conditions, could play a significant role in increasing
523 the solubility of elemental iron in mineral dust aerosols over coastal Namibia. This is in agreement
524 with the mechanism described by Zhuang et al. (1992), who proposed an increase of iron dissolution
525 by the acidification of aerosol particles associated with DMS oxidation, and Johansen and Key (2006),
526 who showed an increase of dissolution of ferrihydrite, a proxy of iron(oxy)hydroxide found in desert
527 mineral dust, by photolysis of the Fe(III)-MSIA (methane sulfinic acid) complex, producing MSA and
528 soluble Fe. It is interesting to note that due to the high correlation between %SFe and %SAI and %SSi
529 (and %STi), the same photochemical processes could also impact the solubility of all element-bearing
530 dust. The possible mechanism suggested by this paper could be responsible for initiating a feedback
531 loop whereby the input of dust of increased trace and major elements solubility would result in stronger
532 marine biogenic emissions to the atmosphere. This possible mechanism could increase the iron sol-
533 ubility in mineral dust, maybe also initiating a feedback loop whereby the input of dust of increased
534 solubility would result in stronger marine biogenic emissions to the atmosphere, including Volatile
535 Organic Compounds (VOCs), in particular butene, massively emitted by the organisms in the coastal
536 marine foam (Giorio et al., 2022). This complex and dynamic environment where the interplay between
537 the input of atmospheric iron from transported dust and the marine biogenic emissions from the Ben-
538 guela oceanic upwelling system should be further addressed by future research.

539

540 **Data availability.** Original and analysed data are available at the AERIS (<https://aeroclo.aeris->
541 [data.fr/project/](https://aeroclo.aeris-data.fr/project/), last accessed 20/07/2023). The statistical FactoMineR package is available in R (R
542 version 4.1.2, 2021; http://factominer.free.fr/index_fr.html, last accessed 20/07/2023). Meteorological
543 data from the Wlotzkasbaken station (22.31°S, 14.45°E, 73 m asl) are part of the Southern African
544 Science Service Centre for Climate Change and Adaptive Land Management (SASSCAL) Observa-
545 tionNet (<https://www.sasscal.org/>; last accessed 14/04/2023).

546

547 **Author contributions.** PF, DK, SJP, AN, MC, AF and SC prepared and performed the filter sampling.
548 RT, KD, PF, SC, and CMB performed the XRF, IC and ICP analysis of the collected samples. KS and
549 SF performed the model calculations of dust emission fluxes. JPC performed the model calculations
550 of air mass back-trajectories. HA and JC provided with the satellite retrieval of fog and low clouds.
551 PF, KD, RT and SJP analysed and interpreted the dataset. PF and KD wrote the paper with contribu-
552 tions from RT and SJP, and the remaining authors. PF and SJP provided funding. PF coordinated the
553 research activity and supervised its planning and execution.

554

555 **Competing interests.** PF is guest editor for the ACP Special Issue “New observations and related
556 modelling studies of the aerosol–cloud–climate system in the Southeast Atlantic and southern Africa
557 regions”. The remaining authors declare that they have no conflicts of interests.

558

559 **Special issue statement.** This article is part of the special issue “New observations and related mod-
560 elling studies of the aerosol–cloud–climate system in the Southeast Atlantic and southern Africa re-
561 gions (ACP/AMT inter-journal SI)”. It is not associated with a conference.

562

563 **Acknowledgements.** This work receives funding by the French Centre National de la Recherche
564 Scientifique (CNRS) and the South African National Research Foundation (NRF) through the
565 “Groupement de Recherche Internationale Atmospheric Research in southern Africa and the Indian
566 Ocean” (GDRI-ARSAIO) and the Project International de Coopération Scientifique (PICS) “Long-term
567 observations of aerosol properties in Southern Africa” (contract n. 260888) as well as by the Parte-
568 nariats Hubert Curien (PHC) PROTEA of the French Minister of Foreign Affairs and International De-
569 velopment (contract numbers 33913SF and 38255ZE). D. Klopper acknowledges the financial support
570 of the Climatology Research Group of North-West University and the travel scholarship of the French
571 Embassy in South Africa (internship at LISA in summer 2018). R. Torres-Sánchez acknowledges the
572 Postdoctoral Fellowship Margarita Alsolas (University of Huelva) funded by the Ministry of Universities
573 of Spain (NextGenerationEU). The Southern African Science Service Centre for Climate Change and

574 Adaptive Land Management (SASSCAL) ObservationNet (<https://www.sasscal.org/>) is acknowledged
575 for open-access data provision. The authors would also like to acknowledge the support by the IPGP
576 platform PARI for HR-ICP-MS analysis. F. Lahmidi and Z. Zeng (LISA) are acknowledged for support
577 to the ion chromatography analysis.

578

579 **References**

- 580 Andersen, H. and Cermak, J.: First fully diurnal fog and low cloud satellite detection reveals life cycle in the
581 Namib, *Atmos. Meas. Tech.*, 11, 5461–5470, doi: 10.5194/amt-11-5461-2018, 2018.
- 582 Andersen, H., Cermak, J., Solodovnik, I., Lelli, L. and Vogt, R.: Spatiotemporal dynamics of fog and low clouds
583 in the Namib unveiled with ground- and space-based observations, *Atmos. Chem. Phys.*, 1, 4383–4392, doi:
584 10.5194/acp-19-4383-2019, 2019.
- 585 Andersen, H., Cermak, J., Fuchs, J., Knippertz, P., Gaetani, M., Quinting, J., Sippel, S., and Vogt, R.: Synoptic-
586 scale controls of fog and low-cloud variability in the Namib Desert, *Atmos. Chem. Phys.*, 20, 3415–3438,
587 <https://doi.org/10.5194/acp-20-3415-2020>, 2020.
- 588 Andreae, M. O.: Soot Carbon and Excess Fine Potassium: Long-Range Transport of Combustion-Derived Aer-
589 osols, *Science*, 220, 1148-1151, doi:10.1126/science.220.4602.1148, 1983.
- 590 Andreae, M. O., Elbert, W., and de Mora, S. J.: Biogenic sulfur emissions and aerosols over the tropical South
591 Atlantic: 3. Atmospheric dimethylsulfide, aerosols and cloud condensation nuclei, *J. Geophys. Res.*, 100,
592 11335-11356, <https://doi.org/10.1029/94JD02828>, 1995.
- 593 Annegarn, H.J., van Grieken, R.E., Bibby, D.M. and von Blottnitz, F.: Background Aerosol Composition in the
594 Namib Desert, South West Africa (Namibia), *Atmos. Environ.*, 17, 2045–2053, doi: 10.1016/0004-
595 6981(83)90361-X, 1983.
- 596 Bhattachan, A., D'Odorico, P., Baddock, M.C., Zobeck, T.M., Okin, G.S., Cassar, N.: The Southern Kalahari: a
597 potential new dust source in the Southern hemisphere?, *Environ. Res. Lett.*, 7, 024001.
598 <http://dx.doi.org/10.1088/1748-9326/7/2/024001>, 2012.
- 599 Bhattachan, A., P. D'Odorico, and G. S. Okin, Biogeochemistry of dust sources in Southern Africa, *J. Arid En-
600 viron.*, 117, 18-27, <http://dx.doi.org/10.1016/j.jaridenv.2015.02.013>, 2015.
- 601 Baboukas, E. D., Kanakidou, M., and Mihalopoulos, N.: Carboxylic acids in gas and particulate phase above
602 the Atlantic Ocean, *J. Geophys. Res.*, 105, 14459–14471, <https://doi.org/10.1029/1999JD900977>, 2000.
- 603 Baker A.R., T. D. Jickells, M. Witt, and K. L. Linge, Trends in the solubility of iron, aluminium, manganese and
604 phosphorus in aerosol collected over the Atlantic Ocean., *Marine Chem.*, 98, 43-58,
605 <https://doi.org/10.1016/j.marchem.2005.06.004>, 2006.
- 606 Baker, A. R., and T. D. Jickells, Mineral particle size as a control on aerosol iron solubility, *Geophys. Res. Lett.*,
607 33, L17608. <https://doi.org/10.1029/2006GL026557>, 2006.
- 608 Baker, A. R., C. Adams C., T. G. Bell, T. D. Jickells, and L. Ganzeveld, Estimation of atmospheric nutrient inputs
609 to the Atlantic Ocean from 50°N to 50°S based on large-scale field sampling: iron and other dust-associated
610 elements, *Glob. Biogeochem. Cycles*, 27, 755–767, doi:10.1002/gbc.20062, 2013.
- 611 Baker, A. R., M. Thomas, H. W. Bange, and E. Plasencia Sánchez, E., Soluble trace metals in aerosols over
612 the tropical south-east Pacific offshore of Peru, *Biogeosciences*, 13, 817–825, [https://doi.org/10.5194/bg-13-](https://doi.org/10.5194/bg-13-817-2016)
613 817-2016, 2016.

614 Baker, Alex R., et T. D. Jickells, Atmospheric deposition of soluble trace elements along the Atlantic Meridional
615 Transect (AMT), in *The Atlantic Meridional Transect programme (1995-2016)* 158: 41-51.
616 <https://doi.org/10.1016/j.pocean.2016.10.002>, 2017.

617 Baker, A. R., M. Li, and R. Chance, Trace metal fractional solubility in size-segregated aerosols from the tropical
618 eastern Atlantic Ocean, *Global Biogeochemical Cycles*, 34, e2019GB006510.
619 <https://doi.org/10.1029/2019GB006510>, 2020.

620 Bryant, R. G., Bigg, G. R., Mahowald, N. M., Eckardt, F. D., and Ross, S. G., Dust emission response to climate
621 in southern Africa, *J. Geophys. Res.*, 112, D09207, doi:10.1029/2005JD007025, 2007.

622 Caponi, L., Formenti, P., Massabó, D., Di Biagio, C., Cazaunau, M., Pangui, E., Chevaillier, S., Landrot, G.,
623 Andreae, M. O., Kandler, K., Piketh, S., Saeed, T., Seibert, D., Williams, E., Balkanski, Y., Prati, P., and
624 Doussin, J.-F.: Spectral- and size-resolved mass absorption efficiency of mineral dust aerosols in the
625 shortwave spectrum: a simulation chamber study, *Atmos. Chem. Phys.*, 17, 7175–7191,
626 <https://doi.org/10.5194/acp-17-7175-2017>, 2017.

627 Chaboureau, J.-P., L. Labbouz, C. Flamant, and A. Hodzic. Acceleration of the southern African easterly jet
628 driven by radiative effect of biomass burning aerosols and its impact on transport during AEROCLO-sA, *At-
629 mos. Chem. Phys.*, 22, 8639-8658, <https://doi.org/10.5194/acp-22-8639-2022>, 2022.

630 Chance R, T. D. Jickells and A. R. Baker, Atmospheric trace metal concentrations, solubility and deposition
631 fluxes in remote marine air over the south-east Atlantic, *Marine Chemistry*, 177, 45–56, doi:10.1016/j.mar-
632 chem.2015.06.028, 2015.

633 Dansie, A. P., G. F. S. Wiggs, D. S. G. Thomas, and R. Washington, Measurements of windblown dust charac-
634 teristics and ocean fertilisation potential: The ephemeral river valleys of Namibia, *Aeolian Res.*, 29, 30–41,
635 doi:10.1016/j.aeolia.2017.08.002, 2017a.

636 Dansie, A. P., G. F. S. Wiggs, and D. S. G. Thomas, Iron and nutrient content of wind-erodible sediment in the
637 ephemeral river valleys of Namibia, *Geomorphology*, 290, 335-346, <https://doi.org/10.1016/j.geomorph.2017.03.016>, 2017b.

639 Dansie AP, Thomas DSG, Wiggs GFS, Baddock MC, Ashpole I. Plumes and blooms - Locally-sourced Fe-rich
640 aeolian mineral dust drives phytoplankton growth off southwest Africa. *Sci Total Environ.*, doi: 10.1016/j.sci-
641 totenv.2022.154562, 2022.

642 Desboeufs, K. V., R. Losno, et J. L. Colin, Factors influencing aerosol solubility during cloud processes, *Atmos.
643 Environ.*, 35, 3529-3537, [https://doi.org/10.1016/S1352-2310\(00\)00472-6](https://doi.org/10.1016/S1352-2310(00)00472-6), 2001.

644 Desboeufs, K.V., Sofikitis, A., Losno, R., Colin, J.L., Ausset, P. Dissolution and solubility of trace metals from
645 natural and anthropogenic aerosol particulate matter, *Chemosphere* 58, 195–203, 2005.

646 Desboeufs, K., Fu, Y., Bressac, M., Tovar-Sánchez, A., Triquet, S., Doussin, J.F., Giorio, C., Chazette, P.,
647 Disnaquet, J., Feron, A., Formenti, P., Maisonneuve, F., Rodríguez-Romero, A., Zapf, P., Dulac, F., and
648 Guieu, C., Wet deposition in the remote western and central Mediterranean as a source of trace metals to
649 surface seawater, *Atmos. Chem. Phys.*, 22, 2309–2332, <https://doi.org/10.5194/acp-22-2309-2022>, 2022.

650 Eltayeb, M.A.; Van Grieken, R.E., Maenhaut, W. and Annegarn, H.J.: Aerosol-Soil Fractionation for Namib De-
651 sert Samples. *Atmos. Environ.*, 27(5), [https://doi.org/10.1016/0960-1686\(93\)90185-2](https://doi.org/10.1016/0960-1686(93)90185-2), 1993.

652 Feuerstein, S., and Schepanski, K.: Identification of Dust Sources in a Saharan Dust Hot-Spot and Their Imple-
653 mentation in a Dust-Emission Model, *Remote Sensing*, 11, doi:10.3390/rs110100004, 2019.

654 Flamant, C., M. Gaetani, J.-P. Chaboureau, P. Chazette, S. J. Piketh, and P. Formenti. Smoke in the river: an
655 Aerosols, Radiation and Clouds in southern Africa (AEROCLO-sA) case study, *Atmos. Chem. Phys.*, 22,
656 5701–5724, <https://doi.org/10.5194/acp-22-5701-2022>, 2022.

657 Formenti, P., Schütz, L., Balkanski, Y., Desboeufs, K., Ebert, M., Kandler, K., Petzold, A., Scheuven, D.,
658 Weinbruch, S., and Zhang, D.: Recent progress in understanding physical and chemical properties of African
659 and Asian mineral dust, *Atmos. Chem. Phys.*, 11, 8231–8256, <https://doi.org/10.5194/acp-11-8231-2011>,
660 2011.

661 Formenti, P., S. Caquineau, K. Desboeufs, A. Klaver, S. Chevallier, E. Journet, J. L. Rajot, Mapping the phys-
662 ico-chemical properties of mineral dust in western Africa: mineralogical composition, *Atmos. Chem. Phys.*, 14,
663 10663-1068, 2014.

664 Formenti, P., Piketh, S. J., Namwoonde, A., Klopper, D., Burger, R., Cazaunau, M., Feron, A., Gaimoz, C.,
665 Broccardo, S., Walton, N., Desboeufs, K., Siour, G., Hanghome, M., Mafwila, S., Omoregie, E., Junkermann,
666 W., and Maenhaut, W.: Three years of measurements of light-absorbing aerosols over coastal Namibia: sea-
667 sonality, origin, and transport, *Atmos. Chem. Phys.*, 18, 17003-17016, [https://doi.org/10.5194/acp-18-17003-](https://doi.org/10.5194/acp-18-17003-2018)
668 2018, 2018.

669 Formenti, P., B. D'Anna, C. Flamant, M. Mallet, S.J. Piketh, K. Schepanski, F. Waquet, F. Auriol, G. Brogniez,
670 F. Burnet, J. Chaboureau, A. Chauvigné, P. Chazette, C. Denjean, K. Desboeufs, J. Doussin, N. Elguindi, S.
671 Feuerstein, M. Gaetani, C. Giorio, D. Klopper, M.D. Mallet, P. Nabat, A. Monod, F. Solmon, A. Namwoonde,
672 C. Chikwililwa, R. Mushi, E.J. Welton, and B. Holben, The Aerosols, Radiation and Clouds in Southern Africa
673 Field Campaign in Namibia: Overview, Illustrative Observations, and Way Forward, *Bull. Amer. Meteor. Soc.*,
674 100, 1277–1298, <https://doi.org/10.1175/BAMS-D-17-0278.1>, 2019.

675 Gao, Y., Xu, G., Zhan, J., Zhang, J., Li, W., Lin, Q., Chen, L., and Lin, H., Spatial and particle size distributions
676 of atmospheric dissolvable iron in aerosols and its input to the Southern Ocean and coastal East Antarctica,
677 *J. Geophys. Res.*, 118, 12,634–12,648, doi:10.1002/2013JD020367, 2013.

678 Gili, S., Vanderstraeten, A., Chaput, A., King, J., Gaiero, D. M., Delmonte, B., Vallelonga, Paola Formenti,
679 Claudia Di-Biagio, Mathieu Cazaunau, Edouard Pangui, Jean-Francois Doussin, Mattielli, N., South African
680 dust contribution to the high southern latitudes and East Antarctica during interglacial stages, *Communications*
681 *Earth & Environment*, 3, 129, <https://doi.org/10.1038/s43247-022-00464-z>, 2022.

682 Ginoux, P., Prospero, J.M., Gill, T.E., Hsu, N.C., Zhao, M.: Global-scale attribution of anthropogenic and natural
683 dust sources and their emission rates based on MODIS Deep Blue aerosols products, *Rev. Geophys.*, 50,
684 RG3005, doi:10.1029/2012RG000388, 2012.

685 Giorio, C., Doussin, J.F., D'Anna, B., Mas, S., Filippi, D., Denjean, C., Mallet, M.D., Bourriane, T., Burnet, F.,
686 Cazaunau, M., Chikwililwa, C., Desboeufs, K., Feron, A., Michoud, V., Namwoonde, A., Andreae, M.O., Piketh,

687 S.J. and Formenti, P.: Butene emissions from coastal ecosystems may contribute to new particle formation,
688 *Geophys. Res. Lett.*, 49, <https://doi.org/10.1029/2022GL098770>, 2022.

689 Grini, A., Tulet, P., and Gomes, L.: Dusty weather forecasts using the MesoNH mesoscale atmospheric model.
690 *J. Geophys. Res.*, 111, D19205, <https://doi.org/10.1029/2005JD007007>, 2006.

691 Hamilton, D. S., Perron, M.M.G., Bond, T.C., Bowie, A.R., Buchholz, R.R., Guieu, C., Ito, A., Maenhaut, W.,
692 Myriokefalitakis, S., Olgun, N., Rathod, S.D., Schepanski, K., Tagliabue, A., Wagner, R. and Mahowald, N.M.:
693 Earth, wind, fire, and pollution: Aerosol nutrient sources and impacts on ocean biogeochemistry, *Annual re-*
694 *view of Marine Science*, 14, pp. 303- 330, <https://doi.org/10.1146/annurev-marine-031921-013612>, 2021.

695 Heike, K and J. Volkel, Soil clay minerals in Namibia and their significance for the terrestrial and marine past
696 global change, *African Study Monographs, Suppl.40*, 2010.

697 Heimburger, A., Losno, R., and Triquet, S.: Solubility of iron and other trace elements in rainwater collected on
698 the Kerguelen Islands (South Indian Ocean), *Biogeosciences*, 10, 6617–6628, [https://doi.org/10.5194/bg-10-](https://doi.org/10.5194/bg-10-6617-2013)
699 [6617-2013](https://doi.org/10.5194/bg-10-6617-2013), 2013.

700 Hooper, H., Mayewski, P., Marx, S., Henson, S., Potocki, M., Sneed, S., Handley, M., Gasso, S., Fischer, M.,
701 Saunders, K.M., Examining links between dust deposition and phytoplankton response using ice cores. *Aeo-*
702 *lian Res.*, 36, 45-60, <https://doi.org/10.1016/j.aeolia.2018.11.001>, 2019.

703 Ito, A., and Kok, J. F.: Do dust emissions from sparsely vegetated regions dominate atmospheric iron supply to
704 the Southern Ocean?, *J. Geophys. Res.*, 122, 3987-4002, <https://doi.org/10.1002/2016JD025939>, 2017.

705 Ito, A., Y. Ye, C. Baldo, and Z. Shi, Ocean Fertilization by Pyrogenic Aerosol Iron. *npj Climate Atmos. Sci.*, 4,
706 30, doi: 10.1038/s41612-021-00185-8, 2021.

707 Jickells, T., Andersen, K.K., Baker, A., Bergametti, G., Brooks, N., Cao, J., Boyd, P., Duce, R., Hunter, K.,
708 Global iron connections between desert dust, ocean biogeochemistry, and climate, *Science*, 308, 67-71, DOI:
709 10.1126/science.1105959, 2005.

710 Journet, E., Desboeufs, K., Caquineau, S. and Colin, J. L.: Mineralogy as a critical factor of dust iron solubility,
711 *Geophys. Res. Lett.*, 35, <https://doi.org/10.1029/2007GL031589>, 2008.

712 Johansen, A. M., and Key, J. M.: Photoreductive dissolution of ferrihydrite by methanesulfinic acid: Evidence of
713 a direct link between dimethylsulfide and iron-bioavailability, *Geophys. Res. Lett.*, 33, L14818,
714 doi:10.1029/2006GL026010, 2006.

715 Kaplan, J.O., Bigelow, N.H., Prentice, I.C., Harrison, S.P., Bartlein, P.J., Christensen, T.R., Cramer, W., Matve-
716 yeva, N.V., McGuire, A.D., Murray, D.F., Razzhivin, V.Y., Smith, B., Walker, D.A., Anderson, P.M., Andreev,
717 A.A., Brubaker, L.B., Edwards, M.E. and Lozhkin A.V.: Climate change and Arctic ecosystems: 2. Modeling,
718 paleodata-model comparison and future projections, *J. Atmos. Res.*, 108, 8171, doi: 10.1029/2002JD002559,
719 2003.

720 Kanguuehi, K. I., Southern African dust characteristics and potential impacts on the surrounding oceans, PhD
721 Thesis, Stellenbosch University, <http://hdl.handle.net/10019.1/123923>, 2021.

722 Klopfer, D., Formenti, P., Namwoonde, A., Cazaunau, M., Chevaillier, S., Feron, A., Gaimoz, C., Hease, P.,
723 Lahmidi, F., Mirande-Bret, C., Triquet, S., Zeng, Z. And Piketh, S.J.: Chemical composition and source apportionment of atmospheric aerosols on the Namibian Coast, *Atmos. Chem. Phys.*, 20, pp. 15811 – 15833,
724 <https://doi.org/10.5194/acp-20-15811-2020>, 2020.

726 Kok, J. F., Albani, S., Mahowald, N. M., and Ward, D. S.: An improved dust emission model – Part 2: Evaluation
727 in the Community Earth System Model, with implications for the use of dust source functions, *Atmos. Chem. Phys.*, 14, 13043–13061, <https://doi.org/10.5194/acp-14-13043-2014>, 2014.

729 Kok, J.F., Ridley, D.A., Zhou, Q., Miller, R.L., Zhao, C., Heald, C.L., Ward, D.S., Albani, S., Haustein, K.: Smaller
730 desert dust cooling effect estimated from analysis of dust size and abundance. *Nature Geoscience*, 10, 274–
731 278, <https://doi.org/10.1038/ngeo2912>, 2017.

732 Laurent, B., Marticorena, B., Bergametti, G., Chazette, P., Maignan, F. and Schmechtig C.: Simulation of the
733 mineral dust emission frequencies from desert areas of China and Mongolia using an aerodynamic roughness
734 length map derived from POLDER/ADEOS 1 surface products, *J. Geophys. Res.*, 110, D18, doi:
735 10.1029/2004JD005013, 2005.

736 Lide, D. R.: *CRC Handbook of Chemistry and Physics 1991–1992*, CRC Press, Boca Raton, Florida, 1992.

737 Liu, M., Matsui, H., Hamilton, D.S., Lamb, K.D., Rathod, S.D., Schwarz, J.P. and Mahowald, N.M.: The underap-
738 preciated role of anthropogenic sources in atmospheric soluble iron flux to the Southern Ocean, *Climate At-
739 mos. Sci.*, 5, 28, <https://doi.org/10.1038/s41612-022-00250-w>, 2022.

740 Longo, A., F. Y. Feng, B., W. M. Landing, R.U. Shelley, A. Nenes, N. Mihalopoulos, K. Violaki, E. D. Ingall.
741 Influence of Atmospheric Processes on the Solubility and Composition of Iron in Saharan Dust, *Environ. Sci.
742 Tech.*, 50, 13: 6912-20. <https://doi.org/10.1021/acs.est.6b02605>, 2016.

743 Mahowald, N., Luo, C., del Corral, J., Zender, C.S.: Interannual variability in atmospheric mineral aerosols from
744 a 22-year model simulation and observational data, *J. Geophys. Res.*, 108 (D12),
745 <https://doi.org/10.1029/2002JD002821>, 2003.

746 Marcotte, A.R., Anbar, A.D., Majestic, B.J., Herckes, P.: Mineral dust and iron solubility: Effects of composition,
747 particle size, and surface area, *Atmosphere*, 11, 533, doi:10.3390/atmos11050533, 2020.

748 Marticorena, B. and Bergametti, G.: Modelling the atmospheric dust cycle: 1. Design of a soil-derived dust
749 emission scheme, *J. Geochem. Res.*, 16415-16430, 1995.

750 Marticorena, B., Chazette, P., Bergametti, G., Dulac, F., Legrand, M.: Mapping the aerodynamic roughness
751 length of desert surfaces from the POLDER/ADEOS bi-directional reflectance product, *Int. J. Remote Sens.*,
752 25, 603– 626, 2004.

753 Myriokefalitakis, S., Tsigaridis, K., Mihalopoulos, N., Sciare, J., Nenes, A., Kawamura, K., Segers, A., and
754 Kanakidou, M.: In-cloud oxalate formation in the global troposphere: a 3-D modeling study, *Atmos. Chem.
755 Phys.*, 11, 5761-5782, doi:10.5194/acp-11-5761-2011, 2011.

756 Paris, R., Desboeufs, K. V., Formenti, P., Nava, S., and Chou, C.: Chemical characterisation of iron in dust and
757 biomass burning aerosols during AMMA-SOP0/DABEX: implication for iron solubility, *Atmos. Chem. Phys.*,
758 10, 4273–4282, <https://doi.org/10.5194/acp-10-4273-2010>, 2010.

759 Paris, R., K.V. Desboeufs, et E. Journet. Variability of dust iron solubility in atmospheric waters: Investigation of
760 the role of oxalate organic complexation, *Atmos. Environ.*, 45, 6510-17. <https://doi.org/10.1016/j.atmosenv.2011.08.068>, 2011.

762 Paris, R., and K. V. Desboeufs, Effect of atmospheric organic complexation on iron-bearing dust solubility. *Atmos. Chem. Phys.*, 13, 4895-4905, <https://doi.org/10.5194/acp-13-4895-2013>, 2013.

764 Perron, M. M. G., Strzelec, M., Gault-Ringold, M., Proemse, B. C., Boyd, P. W., and Bowie, A. R.: Assessment
765 of leaching protocols to determine the solubility of trace metals in aerosols, *Talanta*, 208, 120377,
766 <https://doi.org/10.1016/j.talanta.2019.120377>, 2020.

767 Prospero, J.M., Ginoux, P., Torres, O., Nicholson S.E. and Gill, T.M.: Environmental characterization of global
768 sources of atmospheric soil dust identified with the Nimbus 7 total ozone mapping spectrometer (TOMS) ab-
769 sorbing aerosol product. *Reviews of Geophysics*, 40 (1): 1002, <https://doi.org/10.1029/2000RG000095>, 2002.

770 Redemann, J., Wood, R., Zuidema, P., Doherty, S. J., Luna, B., LeBlanc, S. E., Diamond, M. S., Shinozuka, Y.,
771 Chang, I. Y., Ueyama, R., Pfister, L., Ryoo, J.-M., Dobracki, A. N., da Silva, A. M., Longo, K. M., Kacenelen-
772 bogen, M. S., Flynn, C. J., Pistone, K., Knox, N. M., Piketh, S. J., Haywood, J. M., Formenti, P., Mallet, M.,
773 Stier, P., Ackerman, A. S., Bauer, S. E., Fridlind, A. M., Carmichael, G. R., Saide, P. E., Ferrada, G. A., Howell,
774 S. G., Freitag, S., Cairns, B., Holben, B. N., Knobelspiesse, K. D., Tanelli, S., L'Ecuyer, T. S., Dzambo, A. M.,
775 Sy, O. O., McFarquhar, G. M., Poellot, M. R., Gupta, S., O'Brien, J. R., Nenes, A., Kacarab, M., Wong, J. P.
776 S., Small-Griswold, J. D., Thornhill, K. L., Noone, D., Podolske, J. R., Schmidt, K. S., Pilewskie, P., Chen, H.,
777 Cochrane, S. P., Sedlacek, A. J., Lang, T. J., Stith, E., Segal-Rozenhaimer, M., Ferrare, R. A., Burton, S. P.,
778 Hostetler, C. A., Diner, D. J., Seidel, F. C., Platnick, S. E., Myers, J. S., Meyer, K. G., Spangenberg, D. A.,
779 Maring, H., and Gao, L.: An overview of the ORACLES (ObseRvations of Aerosols above CLouds and their
780 intEractionS) project: aerosol–cloud–radiation interactions in the southeast Atlantic basin, *Atmos. Chem.*
781 *Phys.*, 21, 1507–1563, <https://doi.org/10.5194/acp-21-1507-2021>, 2021.

782 Reichholf, J. H., Is Saharan Dust a Major Source of Nutrients for the Amazonian Rain Forest?, *Studies on*
783 *Neotropical Fauna and Environment*, 21:4, 251-255, DOI: 10.1080/01650528609360710, 1986.

784 Rodríguez, S., Prospero, J.M., Lopez-Darias, J., Garcia-Alvarez, M.I., Zuidema, P., Nava, S., Lucarelli, F., Gas-
785 ton, C.J., Galindo, L., Sosa, E.: Tracking the changes of iron solubility and air pollutants traces as African dust
786 transits the Atlantic in the Saharan dust outbreaks. *Atmos. Environ.*, 246, 118092, <https://doi.org/10.1016/j.atmosenv.2020.118092>, 2021.

788 Rodríguez, S., Riera, R., Fonteneau, A., Alonso-Pérez, S., and López-Darias, J.: African desert dust influences
789 migrations and fisheries of the Atlantic skipjack-tuna, *Atmospheric Environment*, 312, 120022,
790 <https://doi.org/10.1016/j.atmosenv.2023.120022>, 2023.

791 Shelley, R.U., Morton, P.L., Landing, W.M., Elemental ratios and enrichment factors in aerosols from the US-
792 GEOTRACES North Atlantic transects. *Deep-Sea Res. II*, 2014.

793 Shelley, R. U., Landing, W. M., Ussher, S. J., Planquette, H., & Sarthou, G. Regional trends in the fractional
794 solubility of Fe and other metals from North Atlantic aerosols (GEOTRACES cruises GA01 and GA03) follow-
795 ing a two-stage leach, *Biogeosciences*, 15(8), 2271–2288. <https://doi.org/10.5194/bg-15-2271-2018>, 2018.

796 Sholkovitz, E.R., Sedwick, P.N., Church, T.M. Influence of anthropogenic combustion emissions on the deposi-
797 tion of soluble aerosol iron to the ocean: empirical estimates for island sites in the North Atlantic, *Geochim.*
798 *Cosmochim. Acta*, 73, 3981–4003, <http://dx.doi.org/10.1016/j.gca.2009.04.029>, 2009.

799 Siefert, R. L., S. O. Pehkonen, Y. Erel, and M. R. Hoffman, Iron photochemistry of aqueous suspensions of
800 ambient aerosol with added organic acids, *Geochim. Cosmochim. Acta*, 58, 3271–3279, 1994.

801 Spirig, R., Vogt, R., Larsen, J. A., Feigenwinter, C., Wicki, A., Franceschi, J., Parlow, E., Adler, B., Kalthoff, N.,
802 Cermak, J., Andersen, H., Fuchs, J., Bott, A., Hacker, M., Wagner, N., Maggs-Kölling, G., Wassenaar, T. and
803 Seely, M.: Probing the fog life-cycles in the Namib desert, *Bull. Am. Met. Soc.*, 100, 2491-2508,
804 [doi:10.1175/bams-d-18-0142.1](https://doi.org/10.1175/bams-d-18-0142.1), 2019.

805 Swan, H.B., and J. P. Ivey, Elevated particulate methanesulfonate, oxalate and iron over Sydney Harbour in the
806 austral summer of 2019-20 during unprecedented bushfire activity, *Atmos. Environ.*, 226, 118739,
807 <https://doi.org/10.1016/j.atmosenv.2021.118739>, 2021.

808 Swap, R., Garstang, M., Macko, S.A., et al., The long-range transport of southern African aerosols to the tropical
809 South Atlantic. *J. Geophys. Res.*, 101, 23777–23791, <https://doi.org/10.1029/95jd01049>, 1996.

810 Takahashi, Y., Higashi, M., Fukurawa, T., Mitsunobu, S.: Change of iron species and iron solubility in Asian
811 dust during the long-range transport from western China to Japan, *Atmos. Chem. Phys*, 11, 11237-11252,
812 [doi:10.5194/acp-11-11237-2011](https://doi.org/10.5194/acp-11-11237-2011), 2011.

813 Tao, Y., Murphy, J.G.: The mechanisms responsible for the interactions among oxalate, pH, and Fe dissolution
814 in PM_{2.5}. *Earth and Space Chemistry*, 3, 2259-2265, <https://doi.org/10.1021/acsearthspacechem.9b00172>,
815 2019.

816 Tegen, I., Schepanski, K.: The Global distribution of Mineral Dust, *IOP Conference Series: Earth and Environ-*
817 *mental Sciences*, 7, 012001, [doi:10.1088/1755-1307/7/1/012001](https://doi.org/10.1088/1755-1307/7/1/012001), 2009.

818 Tyson, P. D. and Preston-Whyte, R. A.: *The Weather and Climate of Southern Africa*, 2nd ed., Oxford University
819 Press Southern Africa, Cape Town, 2014.

820 Ventura, A., Simões, E.F.C., Almeida, A.S., Martins, R., Duarte, A.C., Loureiro, S., Duarte, R.M.B.O., Deposition
821 of aerosols onto upper ocean and their impacts on marine biota, *Atmosphere*, 12, 684,
822 <https://doi.org/10.3390/atmos12060684>, 2021.

823 Vickery, K.J., Eckardt, F.D.: Dust emission controls on the lower Kuiseb River valley, Central Namib, *Aeolian*
824 *Res.*, 10, 125-133, <https://doi.org/10.1016/j.aeolia.2013.02.006>, 2013.

825 von Holdt, J.R., Eckardt, F.D., Wiggs, G.F.S.: Landsat identifies aeolian dust emission dynamics at the landform
826 scale, *Remote Sensing Environ.*, 198, 229-243, <https://doi.org/10.1016/j.rse.2017.06.010>, 2017.

827 Wozniak, A. S.; Shelley, R. U.; Sleighter, R. L.; Abdulla, H. A. N.; Morton, P. L.; Landing, W. M.; Hatcher, P. G.
828 Relationships among aerosol water soluble organic matter, iron and aluminium in European, North African,

829 and Marine air masses from the 2010 US GEOTRACES cruise, *Mar. Chem.*, 154, 24– 33 DOI: 10.1016/j.mar-
830 chem.2013.04.011, 2013.

831 Wozniak, A. S., R.U. Shelley, S.D. McElhenie, W.M. Landing, P. G. Hatcher. Aerosol water soluble organic
832 matter characteristics over the North Atlantic Ocean: Implications for iron-binding ligands and iron solubility.
833 SCOR WG 139: Organic Ligands – A Key Control on Trace Metal Biogeochemistry in the Ocean 173: 162-72.
834 <https://doi.org/10.1016/j.marchem.2014.11.002>, 2015.

835 Zhuang, G., Z. Yi, R. A. Duce, and Brown, P.R.: Link between iron and sulphur cycles suggested by detection
836 of Fe (II) in remote marine aerosols, *Nature*, 355, pp. 537–539, <https://doi.org/10.1038/355537a0>, 1992.

837

838